Title
Hundreds-fold Sensitivity Enhancement of Photothermal Microscopy in Near-Critical Xenon

Journal
The Journal of Physical Chemistry Letters, 7(13)

ISSN
1948-7185

Authors
Ding, Tina X
Hou, Lei
van der Meer, Harmen
et al.

Publication Date
2016-07-07

DOI
10.1021/acs.jpclett.6b00964

Peer reviewed

THE JOURNAL OF PHYSICAL CHEMISTRY Letters

Letter

pubs.acs.org/JPCL

Hundreds-fold Sensitivity Enhancement of Photothermal Microscopy in Near-Critical Xenon

Tina X. Ding,[†,⊥] Lei Hou,[#] Harmen van der Meer,[#] A. Paul Alivisatos,[†,‡,⊥,§] and Michel Orrit*[,#]

[†]Department of Chemistry and [‡]Department of Material Science, University of California, Berkeley, Berkeley, California 94720, United States

[⊥]Material Sciences Division, Lawrence Berkeley National Laboratory, Berkeley, California 94720, United States

[§]Kavli Energy NanoScience Institute, Berkeley, California 94720, United States

[#]Leiden Institute of Physics, Huygens-Kamerlingh Onnes Laboratory, Postbus 9504, 2300 RA Leiden, The Netherlands

Supporting Information

ABSTRACT: Photothermal absorption microscopy of single Au nanoparticles was conducted at temperatures and pressures near the critical point of Xenon (T_c = 16.583 °C, P_c = 5.842 MPa). The divergence of the thermal expansion coefficient at the critical point makes the refractive index highly sensitive to changes in temperature, which directly translates to a large enhancement of the photothermal signal. We find that measurements taken near the critical point of Xe give a signal enhancement factor of up to 440 ± 130 over those taken in glycerol. The highest sensitivity recorded here corresponds to power dissipation of 64 pW, achieving a signal-to-noise ratio of 9.4 for 5 nm Au nanoparticles with an integration time of 50 ms, making this the most sensitive of any absorption microscopy technique reported to date. Enhancing the sensitivity of absorption microscopy lowers the operating heating power, allowing the technique to be more compatible with absorbers with absorption coefficient and photochemical stability lower than that of Au.

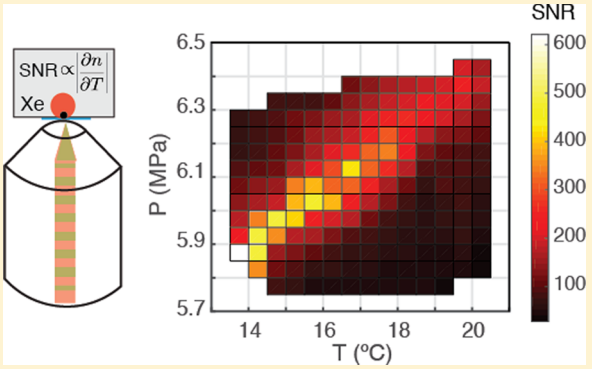

Optical detection of single molecules and nanoparticles has shown tremendous promise in structural biological imaging,[1,2] unraveling kinetic mechanisms of biochemical processes,[3] and advancing fundamental photophysics of molecules and nanoparticles alike.[4−6]

Although the technique was first demonstrated in absorption mode,[7] fluorescence microscopy has instead become the ubiquitous method of choice in detecting single objects for two main reasons: it is background-free and relatively simple to implement. Absorption is an inherently more common and robust process than fluorescence, and it is less sensitive to the environment. However, the detection of absorption via the common method of transmission is at least 10^3 times weaker in sensitivity[8] than fluorescence.

The challenges for observing absorption are further exacerbated when reduced to a single molecule. First, the attenuation of a laser beam by a single molecule is 10^{-7}, much smaller than typical laser fluctuations. Second, the molecule's absorption cross section is one-millionth the area of the narrowest visible beam, meaning the background signal is overwhelming. Traditionally, these challenges were addressed by operating at cryogenic conditions, embedding the molecules in a crystal matrix that acts to spectrally scatter the molecules, and combining a series of lock-in detection techniques.[7]

The past decade has seen many successful efforts to detect single-molecule absorption at room temperature. Photothermal microscopy, a thermo-optical technique that detects non-radiative emission, was the first to do so.[9] A series of papers by Sandoghar and colleagues demonstrated the detection of single-molecule absorption via transmission by using a sophisticated method to reduce laser fluctuations and background.[10,11] In a study by the Xie group, two double-modulated excitation beams were used to detect the depletion of the ground absorption state of the molecule.[12]

Despite this progress, the excitation flux used in all of the mentioned work is 100−1000 times higher than that used in routine single-molecule fluorescence microscopy. Under these conditions, nonequilibrium processes arise, such as triplet−triplet annihilation in molecules[13] and Auger recombination in semiconductor materials.[14] The population of these unstable energy states increases the pathways for chemical photodegradation of the absorber, rendering it unstable for measurement times longer than tens of seconds.[9] In order to study molecules and particles under steady-state conditions for

Received: May 4, 2016
Accepted: June 13, 2016
Published: June 13, 2016

DOI: 10.1021/acs.jpclett.6b00964
J. Phys. Chem. Lett. 2016, 7, 2524−2529

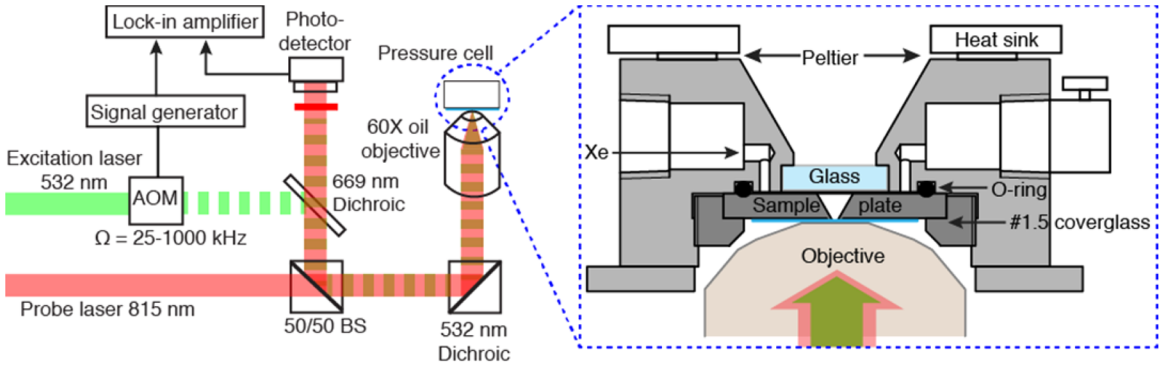

Figure 1. Experimental optical setup with a schematic of the pressure cell.

a prolonged period of time, it is essential to improve the sensitivity of absorption microscopy which would allow us to lower the heating powers used.

Out of all the room-temperature absorption techniques discussed, photothermal microscopy is the most extensively studied, and its theoretical understanding is the most established because of its similarity to other photothermal spectroscopy methods that were studied decades prior.[15]

In this technique, a frequency-modulated heating beam photoexcites the absorber, which releases heat to the surrounding medium via nonradiative relaxation pathways. This heat results in a temperature increase in the region around the absorber, which induces a temporally and spatially varying refractive index change Δn (eq 1). The time-dependent temperature profile in the steady-state regime (eq 2) depends on the important parameters of thermal conductivity (κ), radial distance (r) from the center of the absorber, intensity of the excitation beam (I_{heat}), the absorber's absorption cross section (σ_{abs}), and thermal diffusion length (r_{th}) of the dissipated heat which is given by eq 3 and depends on the modulation frequency (Ω), isobaric heat capacity (C_p), and κ.

$$\Delta n(r, t) = \frac{\partial n}{\partial T}\Delta T(r, t) \tag{1}$$

$$\Delta T(r, t) = \frac{I_{heat}\sigma_{abs}}{4\pi\kappa r}[1 + \exp(-r/r_{th})\cos(\Omega t - r/r_{th})] \tag{2}$$

$$r_{th} = \sqrt{\frac{2\kappa}{\Omega C_p}} \tag{3}$$

In the experimental setup for photothermal microscopy, a probe beam with wavelength outside the absorption window of the particle is focused at the same volume as the heating beam and scattered by the medium's Δn at the same frequency as the heating modulation. The signals are fed into a photodetector, and the component associated with the input frequency is extracted via a lock-in amplifier.

The measured signal therefore depends on the overlap of the probe beam with the volume of thermal dissipation. Specifically, r_{th} should be close to the radius of the probe beam (ω) to obtain the maximal signal detection. Because ω is known for a given wavelength, we can determine the characteristic time constant for thermal relaxation τ (eq 4). Choosing a modulation Ω such that $\Omega\tau \approx 1$, with

$$\tau = \frac{\omega^2 C_p}{2\kappa} \tag{4}$$

we ensure that the probe beam focus is matched to the region where the temperature is effectively modulated.

The interaction of the probe beam with Δn has been previously modeled.[16] The results produce a relationship for the photothermal signal-to-noise ratio (SNR) (eq 5), where $f(\Omega)$ is a function that describes the complex frequency dependence of the signal, which is strongly dependent on r_{th}.

$$\mathrm{SNR} = \frac{1}{\pi\omega_o\lambda^2\Omega}n\left|\frac{\partial n}{\partial T}\right|\frac{1}{C_p}\frac{\sigma_{abs}}{A}P_{heat}\sqrt{\frac{P_{probe}\Delta t}{h\nu}}f(\Omega) \tag{5}$$

To enhance photothermal sensitivity, we exploit the divergent behavior of the thermal expansion coefficient of Xe, α_p, proportional to $\partial\rho/\partial T$ (eq 6; ρ is density). This coefficient's divergence is a fundamental thermodynamic phenomenon at second-order phase transitions in fluids.

$$\alpha_p = -\frac{1}{\rho}\left(\frac{\partial\rho}{\partial T}\right)_p \tag{6}$$

Given density's close relationship with refractive index, n, the thermo-optical parameter $\partial n/\partial T$ in eq 5 also diverges under these conditions, giving rise to the well-known critical opalescence. One can take advantage of this divergence by conducting photothermal microscopy in solvents near the critical point, where $\partial n/\partial T$ is extremely large. Three groups have sought these strategies by exploring photothermal signal enhancement near the thermotropic phase transition of 4-cyano-4′-pentylbiphenyl (5CB) liquid crystals. They measured about a 20-fold signal enhancement factor in this medium over glycerol.[17−19]

Liquid−vapor phase transitions are sharper and therefore have larger $\partial n/\partial T$ than thermotropic phase transitions. Past work in photothermal deflection spectroscopy, a bulk photothermal technique that abides by the same thermo-optical concept, using supercritical fluids CO_2 and Xe as solvents enhanced the photothermal signal by a factor of 100−1000.[20,21] In this Letter, we demonstrate this concept for photothermal microscopy by experimentally measuring the signal of single Au nanoparticles (NPs) near the critical point of Xe (T_c = 16.583 °C, P_c = 5.842 MPa).

Xenon was chosen for its relatively achievable critical pressure and temperature compared to other common gases and for its relatively low κ and C_p.[22] For example, Xe has κ and C_p values that are more than 10-fold lower than those of CO_2, another chemical with critical point near that of Xe. Equations 2 and 5 indicate that lower values of C_p and κ generally improve the photothermal signal and therefore are desirable.

DOI: 10.1021/acs.jpclett.6b00964
J. Phys. Chem. Lett. 2016, 7, 2524−2529

The optical setup for our experiments is similar to that described in a previous paper (Figure 1).[23] The heating beam (532 nm) and the probe beam (815 nm) are focused and overlapped onto the Au NP to achieve the photothermal signal. The primary novelty of our work is the pressure cell (Figure 1), which was designed and machined based on a previous report.[24] Single Au NPs were spin-coated on a 0.17 mm thick coverglass, which was then glued via Atomic Adhesive AA-BOND F113 epoxy to a stainless steel plate, giving an optical aperture that is 0.7 mm in diameter. The plate was pushed up against an O-ring inside the pressure chamber to seal the cell. This design allowed us to use a high numerical aperture objective while also operating up to 6.4 MPa of pressure without coverglass rupture. Peltier elements and a heat sink were added to the top of the cell for maintaining temperature control. This pressure cell was connected to one side of a 500 ml volume piston, and the pressure of the Xe was regulated by controlling the pressure of nitrogen gas connected to the other side of the piston. Further dimensions of the cell and details on the design of the entire pressure system are described in the Supporting Information.

To predict the photothermal signal response to conditions near the critical point, we have compiled thermodynamic values of density, temperature, pressure, C_p, and κ for Xe at standard temperature and pressure (STP) to near critical point from past literature.[25−27] We present the divergence of α_p, C_p, and κ in informative plots in Figure 2. Complementary to Figure 2 is Table 1, which compares the values of the thermodynamic parameters relevant in this Letter for STP Xe, critical Xe, and glycerol. Refractive index, n, was related to density via the Lorentz−Lorenz relationship, using the reported Lorentz−Lorenz parameter of 10.5 cm^3/mol for the range of temperature and pressure investigated in this study.[28] The thermo-optical relationship between n and temperature for Xe is then illustrated in Figure 2a, which resembles the pressure−density−temperature surface in the vicinity of the critical point. From the figure, we also see that n of Xe approaches a maximum value of 1.2 at our thermodynamic operating range, which is a larger index mismatch with glass than glycerol (n = 1.47). From the fitted data in Figure 2a, we can obtain $\partial n/\partial T$ for this same region, shown in Figure 2b. As conditions tend to the critical point, the values of $\partial n/\partial T$ become not only larger but also more sensitive to small changes in temperature and pressure, as depicted by the narrow temperature width of $\partial n/\partial T$ at 5.8 MPa.

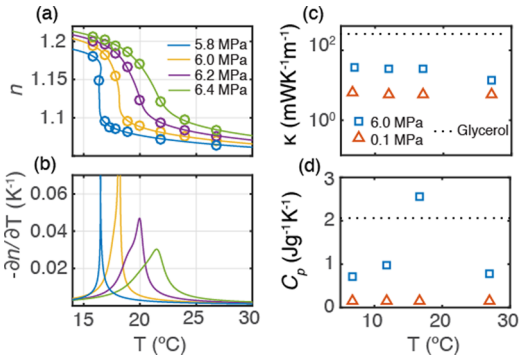

Figure 2. Predicted divergence of thermodynamic parameters near the critical point of Xe. (a) Density-refractive index n diagram extrapolated from density−pressure relationship for Xe at conditions around the critical point. The raw data (circles) were fitted to a fifth-order polynomial (lines). (b) Plot of the derivative of the curve fit from panel a, to obtain $\partial n/\partial T$ over the same region. Note the sharp rise in $\partial n/\partial T$ and increasing narrowness of the curves close to the critical point. (c) Thermal conductivity κ at atmospheric pressure versus 6 MPa. The dashed line indicates glycerol's κ at STP. (d) Heat capacity C_p over the same conditions. The legend is the same as that in panel c.

Table 1. Values of Relevant Thermodynamic Parameters of Glycerol and Xe from refs 25, 28, and 31[a]

	units	glycerol	Xe_{STP}	Xe_{crit}
n		1.473	1	1.138
κ	$mW{\cdot}m^{-1}{\cdot}K^{-1}$	290	5.4	28.9
C_p	$J{\cdot}g^{-1}{\cdot}K^{-1}$	2.06	0.16	2.55
$\lvert\partial n/\partial T\rvert$	K^{-1}	2.7×10^{-4}	5×10^{-6}	$\sim 4 \times 10^{-2}$

[a] $\lvert\partial n/\partial T\rvert$ for Xe_{crit} approximated from Figure 2b.

The dependences of C_p and κ on temperature and pressure, which also affect the photothermal SNR (eq 5), are shown in Figure 2c,d. Divergence of C_p and κ are theoretically predicted at the critical point.[22] However, because of sparse existing experimental data on C_p and κ near the critical point of Xe[25] and the different critical exponents of C_p and κ,[29,30] the divergence is not clearly evident from Figure 2c,d.

We further note that conditions below the critical point might appear to lead to a high photothermal signal because of the density discontinuity across the gas−liquid coexistence (saturation) curve. However, the creation of bubbles across a gas−liquid interface requires large excess heating and a nucleation process that is highly nonlinear and difficult to control.[23] We therefore limit our discussion to near critical states that have high but continuous $\partial n/\partial T$.

We measured the signal-to-noise ratio (SNR) of 20 nm Au NPs over a range of temperatures and pressures extending from below to above the critical point of Xe, at a heating power of 3.5 μW and probe power of 0.6 mW. The heating laser at 532 nm excites the surface plasmon resonance of Au NPs, whose absorbed energy then dissipates into the environment as heat. The data presented in Figure 3 were obtained on three particles and then normalized appropriately to represent the mean of a distribution of 90 Au NPs whose signals we measured at one T, P condition. We then performed an interpolation of the data set to create a continuous two-dimensional map (Figure 3a) of the SNR. Figure 3b shows the interpolated map and the measured data set plotted together in the same three-dimensional (3D)-rendered version of Figure 3a. In the map, the highest signals traverse along a diagonal path, increasing toward the bottom left corner of the map.

The area of the highest thermodynamic sensitivity, and therefore critical divergence, has many unique experimental features. It should have the largest signal, the largest slope, and the largest signal dependence on modulation frequency in the frequency range of 25 kHz to 1 MHz. The first two behaviors are well-depicted by the predictions in Figure 2b, caused by the divergence of α_p. The high modulation frequency dependence stems from the divergence of the characteristic thermal time constant τ coupled with the increase in the correlation lengths associated with critical phenomena.

Maximum SNR as a function of temperature is plotted in Figure 3c, showing that the highest values were achieved in the range of 13.5−15.5 °C and 5.85−6.01 MPa. Although similar SNR values were achieved at three different conditions (Figure

DOI: 10.1021/acs.jpclett.6b00964
J. Phys. Chem. Lett. 2016, 7, 2524−2529

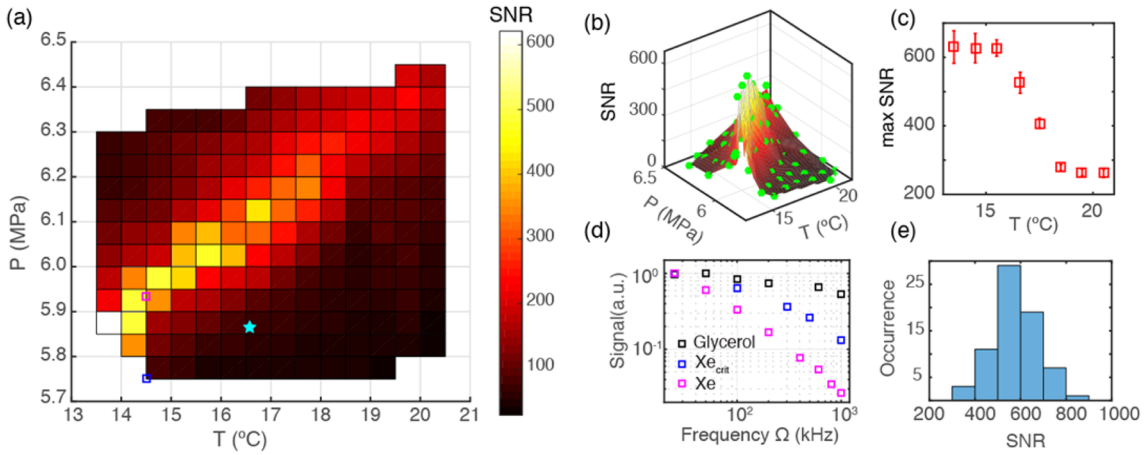

Figure 3. (a) Map of photothermal SNR of 20 nm Au NPs as a function of temperature and pressure from 13.5 to 20.5 °C and 5.7 to 6.4 MPa, respectively, taken at P_{heat} = 3.5 μW and P_{probe} = 600 μW. The map is the interpolation of the collected data, which is shown by green points in panel b. The cyan star indicates the critical point of Xe. Panel b is the 3D interpolated surface of panel a with experimentally measured data plotted in green. (c) Max SNR collected at eight different temperatures measured. Error bars here represent the noise in the measurement, which tends to larger values as the thermodynamic sensitivity becomes very high. (d) Signal response to modulation frequency for glycerol and Xe. The colors for Xe correspond to the thermodynamic conditions indicated by the same colors in panel a. (e) Sampling over 90 particles, we find that the average max SNR in the map is 620, and the standard deviation from the size distribution is 140.

Table 2. Experimental Comparison of SNR of An NPs in Glycerol and Xe

	Au(d)	P_{heat}	P_{probe}	ΔT (K)	P_{diss}	SNR	SNR_{norm} [a]
glycerol	20 nm	210 μW	9.4 mW	14	492 nW	312 ± 50	1
Xe	20 nm	3.5 μW	0.6 mW	2.2	8 nW	620 ± 140	480
glycerol	5 nm	210 μW	20 mW	0.84	7.5 nW	11.4 ± 2.6	0.025
Xe	5 nm	1.8 μW	1 mW	0.057	64 pW	9.4 ± 2.7	10.8

[a] $SNR_{norm} = \frac{SNR}{P_{heat}\sqrt{P_{probe}}} / \frac{SNR_{gly-20nm}}{P_{heat}\sqrt{P_{probe}}}$

3c), the signal at 13.5 °C exhibits a larger slope than the signal at 15.5 °C. Specifically, average SNR of 630 at 13.5 °C and 5.85 MPa drops by a factor of 2 over a pressure change of only 0.02 MPa. As a comparison, at 15.5 °C and 6.01 MPa, we measure similar SNR, but its slope is much smaller, as the signal decreases by a factor of 2 over 0.06 MPa. Because the accuracy of our pressure transducer is 0.025 MPa and we are not using a sophisticated system to maintain precise pressure and temperature conditions down to kilopascal and millikelvin,[21] the signals at these highly sensitive regions will be large but noisy. The error bars in the Figure 3c represent the noise associated with the sensitivity and slope, which noticeably becomes largest at 13.5 °C.

A comparison of signal dependence on modulation frequency for Au in a highly diverging Xe (magenta box in Figure 3a) environment, a more weakly diverging Xe (black) environment, and glycerol is plotted in Figure 3d. The sharpest drop-off seen for highly diverging Xe is indicative of the increase in the characteristic thermal time constant τ, or likewise, the decrease in the thermal diffusion length r_{th}. Specifically, inputting reported values of C_p and κ for glycerol and critical Xe, we find that from 25 kHz to 1 MHz, r_{th} spans from 780 to 120 nm for critical Xe while it spans from 3 μm to 470 nm for glycerol (compared to $\omega \approx 250$ nm). We therefore attribute the complex frequency dependence of the photothermal signal in near-critical Xe to the large ranges of spatial and temporal fluctuations close to the critical point.

There exists some discrepancy between the predicted and experimental region at which the maximum enhancement occurs. Figure 3a shows that the highest sensitivity occurs at temperatures lower than T_c and pressure higher than P_c (critical point is represented by the cyan star in Figure 3a). We believe that both discrepancies may arise in part from the purity of the Xe gas and in part from local heating by pump and probe beams, which removes fluid layers close to the particle from critical conditions. The change in temperature at the surface of the 20 nm Au NP is around 2.2 K (Table 2). Given the high sensitivity of the signal to changes in temperature and pressure as discussed in the previous paragraphs, the local temperature at the surface of the particle is likely higher than the temperature readout in our data. Therefore, one would need to go to lower temperature than T_c to achieve temperature that is near T_c in the vicinity of the thermo-optical enhancement. Impure Xe also leads to its effective critical point shifting to higher pressure and lower temperature, as well as weaker divergence. One possible source of impurity in the Xe gas may be the effectiveness of the piston separating N_2 gas from Xe. Indeed, we find that the more the Xe is reused, the more the diagonal path in Figure 3a shifts toward the direction of higher pressure and lower temperature on the map. Furthermore, the modulation frequency dependence of the highest signal in the more impure Xe is weaker than that in a fresh batch of Xe, indicative of the weaker divergence.

We measured and compared the SNR of 5 and 20 nm Au in glycerol and Xe, shown in Table 2. The discrepancy in SNR for 20 and 5 nm particles for each solvent matches the difference in their absorption cross-section within error. Because experiments in glycerol and Xe differ so much in the heating and probe powers used, we calculated the enhancement factor by taking the measurements at the conditions as reported in Table 2 and then normalizing by the linear and square root

DOI: 10.1021/acs.jpclett.6b00964
J. Phys. Chem. Lett. 2016, 7, 2524−2529

dependence on P_{heat} and P_{probe}, respectively, of the SNR in eq 5. This power-normalized SNR is further normalized to the power-normalized SNR for 20 nm Au NP in glycerol. These values are reported in the last column of Table 2 to give a clearer comparison between the sensitivity of the measurement in glycerol and Xe. Using this method, we measure an enhancement factor of 440 ± 130 for experiments in critical Xe over that in glycerol. The enhancement is the same within error for both 5 and 20 nm and is similar to the enhancements measured for CO_2 and Xe in photothermal deflection spectroscopy.[20,21]

Notably, 5 nm Au NPs can be detected with SNR of 9.4 at only 1.8 μW of heating power, which is the lowest of any reported in the literature. The operating conditions for similar SNR of 5 nm Au in Xe uses 117 times less heating power and 20 times less probe power than our measurements with glycerol. Photothermal images of 5 nm Au NPs obtained with their different powers in Xe and glycerol are presented side-by-side in panels a and b of Figure 4, respectively. Measurement in

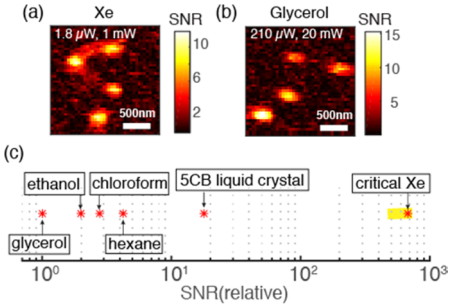

Figure 4. Photothermal image of 5 nm Au NP in Xe (a) and in glycerol (b) under optimal conditions. See Table 2 for parameters used here. The powers listed in the figure correspond to the heating power and the probe power, in that order. (c) Comparison of the relative SNR of Au NPs in Xe, glycerol, common solvents from ref 31, and 5CB liquid crystal from refs 17 and 18.

critical Xe is much more sensitive than in glycerol, being able to detect down to 64 pW in absorbed power. This corresponds to 57 mK of change in temperature at the surface on the 5 nm NPs [amplitude $\Delta T = \sigma_{abs} I_{heat}/(4\pi\kappa r)$]. Figure 4c shows an overall comparison of the normalized SNR obtained using this method with that using glycerol, common solvents,[31] and 5CB liquid crystal as the medium.[17,18] The yellow region indicates the SNR measured without extensive optimization of pressure and temperature. For example, at the temperature of our optics room, 20.5 °C, we can still obtain signal enhancement of up to 260 (Figure 3c).

Again, we stress that all experiments were performed above the critical point, or very close to it, so that no bubble could form around the metal NPs. Although bubbles can lead to large photothermal signals,[23,32] the nucleation process is difficult to control and gives rise to noisy and irreproducible signals that we wished to avoid here. Moreover, bubble formation usually requires significant heating powers, contrary to our aim in the present work.

In conclusion, we have utilized the divergence of the thermal expansion coefficient in critical Xe to achieve a 440-fold improvement in the sensitivity of photothermal microscopy over glycerol, the conventional medium of choice. In theory, any fluids near their critical point should boost the photothermal signal. Besides density divergence, heat capacity and thermal conductivity of the material also exhibit critical divergence and would affect the SNR. Therefore, in choosing a solvent for photothermal microscopy, one must consider not only the practicality of the pressure and temperature operating range for microscopy but also whether these thermodynamic parameters would give thermal diffusion lengths close to the size of the probe beam. Although molecular cell biology is one of the main application fields of photothermal imaging, the present work is not directly relevant to those applications. Rather, we think this method will be useful to study and understand the photophysics of weakly fluorescent or non-fluorescent absorbers by considerably reducing the required heating powers. We hope to demonstrate this in future work.

■ ASSOCIATED CONTENT

Supporting Information

The Supporting Information is available free of charge on the ACS Publications website at DOI: 10.1021/acs.jpclett.6b00964.

Details of the pressure cell design, sample preparation, and additional data (PDF)

■ AUTHOR INFORMATION

Corresponding Author

*E-mail: orrit@physics.leidenuniv.nl.

Notes

The authors declare no competing financial interest.

■ ACKNOWLEDGMENTS

T.X.D. acknowledges the National Science Foundation (NSF) Research Fellowship under Grant DGE 1106400 as well as the joint NSF-NWO program under the Global Research Opportunities Worldwide (GROW) Fellowship. L.H. benefitted from a grant from the Chinese Scholarship Council. We thank Dr. Alexander Gaiduk and Dr. Paul Ruijgrok for pointing out the large enhancement of photothermal coefficients in near-critical fluids.

■ REFERENCES

(1) Hell, S. W. Far-Field. Optical Nanoscopy. *Science* **2007**, *316*, 1153−1158.
(2) Moerner, W. E. Single-Molecule Spectroscopy, Imaging, and Photocontrol: Foundations for Super-Resolution Microscopy (Nobel Lecture). *Angew. Chem., Int. Ed.* **2015**, *54*, 8067−8093.
(3) Tinoco, I. J.; Gonzalez, R. L. J. Biological Mechanisms, One Molecule at a Time. *Genes Dev.* **2011**, *25*, 1205−1231.
(4) Xie, X. S.; Trautman, J. K. Optical Studies of Single Molecules at Room Temperature. *Annu. Rev. Phys. Chem.* **1998**, *49*, 441−480.
(5) Empedocles, S. A.; Neuhauser, R.; Shimizu, K.; Bawendi, M. G. Photoluminescence From Single Semiconductor Nanostructures. *Adv. Mater.* **1999**, *11*, 1243−1256.
(6) Nirmal, M.; Brus, L. Luminescence Photophysics in Semiconductor Nanocrystals. *Acc. Chem. Res.* **1999**, *32*, 407−414.
(7) Moerner, W. E.; Kador, L. Optical-Detection and Spectroscopy of Single Molecules in a Solid. *Phys. Rev. Lett.* **1989**, *62*, 2535−2538.
(8) Lakowicz, J. R. *Principles of Fluorescence Spectroscopy*; Springer: New York, 2006.
(9) Gaiduk, A.; Yorulmaz, M.; Ruijgrok, P. V.; Orrit, M. Room-Temperature Detection of a Single Molecule's Absorption by Photothermal Contrast. *Science* **2010**, *330*, 353−356.
(10) Celebrano, M.; Kukura, P.; Renn, A.; Sandoghdar, V. Single-Molecule Imaging by Optical Absorption. *Nat. Photonics* **2011**, *5*, 95−98.

DOI: 10.1021/acs.jpclett.6b00964
J. Phys. Chem. Lett. 2016, 7, 2524−2529

(11) Kukura, P.; Celebrano, M.; Renn, A.; Sandoghdar, V. Single-Molecule Sensitivity in Optical Absorption at Room Temperature. *J. Phys. Chem. Lett.* **2010**, *1*, 3323−3327.
(12) Chong, S.; Min, W.; Xie, X. S. Ground-State Depletion Microscopy: Detection Sensitivity of Single-Molecule Optical Absorption at Room Temperature. *J. Phys. Chem. Lett.* **2010**, *1*, 3316−3322.
(13) Gaiduk, A.; Yorulmaz, M.; Ishow, E.; Orrit, M. Absorption, Luminescence, and Sizing of Organic Dye Nanoparticles and of Patterns Formed Upon Dewetting. *ChemPhysChem* **2012**, *13*, 946−951.
(14) Berciaud, S.; Cognet, L.; Lounis, B. Photothermal Absorption Spectroscopy of Individual Semiconductor Nanocrystals. *Nano Lett.* **2005**, *5*, 2160−2163.
(15) Bialkowski, S. E. *Photothermal Spectroscopy Methods for Chemical Analysis*; Wiley: New York, 1996.
(16) Berciaud, S.; Lasne, D.; Blab, G. A.; Cognet, L.; Lounis, B. Photothermal Heterodyne Imaging of Individual Metallic Nanoparticles: Theory Versus Experiment. *Phys. Rev. B: Condens. Matter Mater. Phys.* **2006**, *73*, 045424.
(17) Parra-Vasquez, A. N. G.; Oudjedi, L.; Cognet, L.; Lounis, B. Nanoscale Thermotropic Phase Transitions Enhancing Photothermal Microscopy Signals. *J. Phys. Chem. Lett.* **2012**, *3*, 1400−1403.
(18) Chang, W. S.; Link, S. Enhancing the Sensitivity of Single-Particle Photothermal Imaging with Thermotropic Liquid Crystals. *J. Phys. Chem. Lett.* **2012**, *3*, 1393−1399.
(19) Heber, A.; Selmke, M.; Cichos, F. Metal Nanoparticle Based All-Optical Photothermal Light Modulator. *ACS Nano* **2014**, *8*, 1893−1898.
(20) Leach, R. A.; Harris, J. M. Supercritical Fluids as Spectroscopic Solvents for Thermooptical Absorption-Measurements. *Anal. Chem.* **1984**, *56*, 1481−1487.
(21) Briggs, M. E.; Gammon, R. W. Photothermal Deflection in a Supercritical-Fluid. *Int. J. Thermophys.* **1995**, *16*, 1439−1453.
(22) Stanley, H. E. *Introduction to Phase Transitions and Critical Phenomena*; Oxford University Press: New York, 1971.
(23) Hou, L.; Yorulmaz, M.; Verhart, N. R.; Orrit, M. Explosive Formation and Dynamics of Vapor Nanobubbles Around a Continuously Heated Gold Nanosphere. *New J. Phys.* **2015**, *17*, 013050.
(24) Pagliaro, L.; Reitz, F.; Wang, J. An Optical Pressure Chamber Designed for High Numerical Aperture Studies on Adherent Living Cells. *Undersea Hyperbaric Med.* **1995**, *22*, 171−181.
(25) Sifner, O.; Klomfar, J. Thermodynamic Properties of Xenon From the Triple Point to 800-K with Pressures Up to 350-MPa. *J. Phys. Chem. Ref. Data* **1994**, *23*, 63−152.
(26) Hanley, H.; McCarty, R. D.; Haynes, W. M. The Viscosity and Thermal Conductivity Coefficients for Dense Gaseous and Liquid Argon, Krypton, Xenon, Nitrogen, and Oxygen. *J. Phys. Chem. Ref. Data* **1974**, *3*, 979−1018.
(27) Habgood, H. W.; Schneider, W. G. PVT Measurements in the Critical Region of Xenon. *Can. J. Chem.* **1954**, *32*, 98−112.
(28) Garside, D. H.; Molgaard, H. V.; Smith, B. L. Refractive Index and Lorentz-Lorenz Function of Xenon Liquid and Vapour. *J. Phys. B: At. Mol. Phys.* **1968**, *1*, 449−457.
(29) Henry, D. L.; Swinney, H. L.; Cummins, H. Z. Rayleigh Linewidth in Xenon Near the Critical Point. *Phys. Rev. Lett.* **1970**, *25*, 1170−1172.
(30) Smith, I. W.; Giglio, M.; Benedek, G. B. Correlation Range and Compressibility of Xenon Near the Critical Point. *Phys. Rev. Lett.* **1971**, *27*, 1556−1560.
(31) Gaiduk, A.; Ruijgrok, P. V.; Yorulmaz, M.; Orrit, M. Detection Limits in Photothermal Microscopy. *Chem. Sci.* **2010**, *1*, 343−350.
(32) Nedosekin, D. A.; Galanzha, E. I.; Dervishi, E.; Biris, A. S.; Zharov, V. P. Super-Resolution Nonlinear Photothermal Microscopy. *Small* **2014**, *10*, 135−142.

DOI: 10.1021/acs.jpclett.6b00964
J. Phys. Chem. Lett. 2016, 7, 2524−2529